Electronic correlation and Mott localization of paramagnetic CrSBr crystal

L. Craco [1,a], S. S. Carara [1], E. F. Chagas [1], A. R. Cadore [1,2], and S. Leoni [3]

[1] Institute of Physics, Federal University of Mato Grosso, Cuiab´a 78060-900, Brazil
[2] Brazilian Nanotechnology National Laboratory, Campinas 13083-100, Brazil
[3] School of Chemistry, Cardiff University, Cardiff CF10 3AT, UK

Received 13 May 2025 / Accepted 17 June 2025

Abstract. We perform a comprehensive analysis of the correlated electronic structure reconstruction within the paramagnetic phase of CrSBr van der Waals (vdW) crystal. Using generalized gradient approximation plus dynamical mean-field theory calculations, we explicitly demonstrate the importance of local dynamical correlations for a consistent understanding of the emergent Mott localized electronic state, showing the interplay between one-electron lineshape and multi-orbital t_{2g} electronic interactions. Our strongly correlated many-body scenario is relevant to understanding the electronic structure reconstruction of the Cr^{3+} oxidation state with nearly half-filled t_{2g} orbitals and should be applicable to other vdW materials from bulk down to the low-dimensional limit. This work is a step forward in understanding the manifestation of orbital-selective Mott localization and its link to angle-resolved photoemission spectroscopy, electrical resistivity, and the current–voltage characteristic. The presented theoretical results indicate how orbital reconstruction leads to volatile memristive functionality of CrSBr for future neuromorphic computing.

1 Introduction

Since the discovery of two-dimensional (2D) graphene as downscaling layered analog of the bulk, van der Waals (vdW) graphite [1], there has been growing interest in discovering novel layered vdW materials that can be exfoliated and studied at the few-layer or in the 2D limit [2]. Extant works in this field have identified and experimentally realized 2D materials as diverse as metals, insulators, semiconductors, and semimetals systems [3]. Along this line, the finding of magnetic order in 2D magnet materials [4–6] provides an interesting platform to understand and ultimately control low-D magnetism, providing opportunities for atomically thin spintronic, magneto-optic and valleytronic devices [7–9]. To date, however, the growth of bulk vdW materials, from which 2D magnets can be exfoliated, remains challenging due to inadequacies of currently available materials, including low magnetic transition temperatures (T) [4–6], air instability, and poor transport and magnetic properties. In this context, the vdW material CrSBr is expected to be a promising candidate for the realization of a 2D magnetic semiconductor [10–14]. Bulk CrSBr has a high magnetic ordering temperature (N´eel temperature, $T_N \approx 132$ K) [15, 16] compared to the chromium trihalides analogs [17]. Moreover, this layered material shows strong coupling between its electronic and magnetic properties [10, 14]. CrSBr is readily exfoliated down to the 2D limit, and few-layer samples are stable under ambient conditions, making it an interesting candidate for integration into functional vdW heterostructures [13, 18]. This unique combination of physical and chemical properties in a single vdW material has opened great interest in understanding the electronic, optical, and magnetic properties of CrSBr crystals [2].

A Curie–Weiss fit of the magnetic susceptibility gives a Weiss constant of approximately 180 K, indicative of strong ferromagnetic correlations [15]. Further experimental evidences for these high-T ferromagnetic correlations are characterized by two broad features in heat capacity measurements near 185 and 160 K [19] in field dependent magnetization isotherms below 200 K [20] as well as the persistence of magneto-crystalline anisotropy above T_N [21, 22]. Diffuse scattering in single crystal neutron diffraction measurements reveal that these high-T ferromagnetic correlations are confined within the *ab* plane, indicating the predominance of 2D magnetic interactions in the paramagnetic regime [23].

In CrSBr crystal, each layer consists of two buckled rectangular planes of CrS ions, with both surfaces capped by Br atoms [15, 16, 24], see Fig. 1. Stacking of the layers along the *c*-axis gives rise to an orthorhombic structure with space group *Pmmm*. The paramagnetic to antiferromagnetic out-of-plane phase transi-

[a] e-mail: lcraco@fisica.ufmt.br (corresponding author)

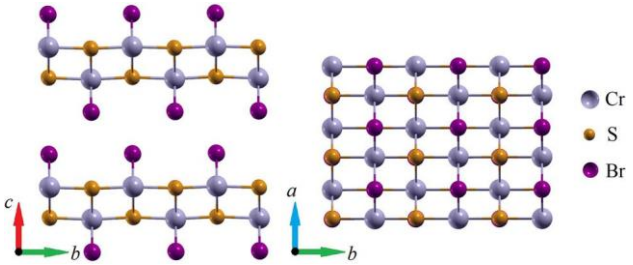

Fig. 1 Schematic representation of the orthorhombic lattice structure of CrSBr bulk crystal

tion includes substantial intralayer ferromagnetic correlations setting in above T_N [14], as seen by heat capacity [18] and magnetic susceptibility [15] measurements. Below T_N, the layers order ferromagnetically, with spins oriented along the b axis, and antiferromagnetically along the stacking direction [15, 16]. Importantly, in bulk single crystals, CrSBr is considered to be a broadband semiconductor with a direct bandgap of 1.5 [15, 25] to 2.0 eV [12], displaying finite conductivity values down to low T [2, 15, 26]. Although magnetic susceptibility [14, 15, 20] and magnetoresistance [14] measurements show two inflection points across the magnetic phase transition, the electrical conductivity and resistance measurements show a nearly continuous T-dependence in Refs. [2, 15, 27], and only recently two inflection points at 40 K and 128 K have been reported [26], meaning that magnetism in CrSBr samples are sensitive to gate voltages and electric field on cooling [27], as well as to electrostatically tunable spin polarization [28]. This sensitivity suggests that in CrSBr, field-driven external perturbations might not only induce magnetic phase transitions, but also nonvolatile resistive switching [27] relevant to neuromorphic computing [29].

To address the electronic structure of magnetic CrSBr systems, ab initio density functional theory (DFT) schemes were performed in recent years [11, 30–32]. These DFT calculations correctly describe the semiconducting electronic state of the magnetically ordered phases with strongly spin and orbital polarized electron bands. Moreover, a perusal of extant DFT+U studies [30, 33, 34], which explicitly take into account the effect of intrinsic electron–electron interactions on a Hartree-like level in the Cr 3d shell, reveals that the on-site Coulomb interaction U for CrSBr could reach values up to 5.0 eV [34]. However, in spite of these theory studies of fundamental importance, the dynamical quantum nature of the paramagnetic electronic state [12, 35] of CrSBr crystals has been largely unexplored. Motivated thereby, in this work we extend our earlier studies on Cr-trihalides [36, 37] to perform a detailed analysis of the electronic structure reconstruction within the paramagnetic phase of CrSBr crystal. Using the DFT plus dynamical mean-field theory (DFT+DMFT) approximation [38], we show the emergent correlated electronic state with distinct orbital-selective many-particle fingerprints. Similar to Ref. [36, 37], our study highlights the importance of incorporating multi-orbital (MO) dynamical correlations within the Cr-t_{2g} orbitals to determine the role played by self-energy corrections to the electronic spectra of this correlated many-particle vdW compound.

2 Theory, results and discussion

The DFT calculations were performed for the nonmagnetic electronic state of orthorhombic CrSBr (see Fig. 1) using the SIESTA ab initio simulation package [39] (code 4.1.5). Generalized gradient approximation (GGA) in the Perdew–Burke–Ernzerhof (PBE) implementation [40] was applied as the exchange correlation functional. Troullier–Martins pseudopotentials [41] in Kleinman–Bylander nonlocal form were used to represent the ionic core potential. The Kohn–Sham orbitals [42] are expanded in a linear combination of atomic orbitals of finite range which is determined by a common confinement energy shift of 0.01 Ry [43]. The precision of the real-space grid integration is determined by an energy cutoff of 200 Ry [44]. The respective Brillouin zone is sampled by a $10 \times 10 \times 10$ Monkhorst-Pack grid [45] for the geometry optimization of a primitive cell of bulk CrSBr. The calculation of density of states was performed usinga $50 \times 50 \times 50$ Monkhorst-Pack grid. All the lattice constants were taken from Ref. [16]. Finally, as in Ref. [36, 37], the atomic positions were fully optimized until all the force components became smaller than 0.03 $\mathrm{eV}/\mathring{A}$.

To begin with, in Fig. 2, we show the orbital-resolved and total GGA density of states (DOS) for t_{2g} orbitals of orthorhombic ($Pmmm$ space group) structural phase of paramagnetic CrSBr bulk crystal relevant to understanding the high-spin state of the Cr^{3+} ($S = 3/2$) ion [30, 33, 46]. Owing to the octahedral environment of the Cr sites, the 3d states split into half-filled [46] t_{2g} and unoccupied [30] e_g orbitals. With these caveats, in Fig. 2, we show the Cr 3d-t_{2g} states of CrSBr near Fermi level, $E_F = \omega = 0$. As frequently found in transition metal compounds, the e_g states are higher in energy and are almost fully polarized in CrSBr, so they will not be considered in our study. More importantly, given the narrow bandwidth of the active t_{2g} orbitals, MO electron–electron interactions will scatter electrons among the t_{2g} channels via the interorbital Coulomb interaction U' and the Hund's exchange parameter J_H [36, 37], inducing clearly visible changes in the bare DFT spectral functions as shown in Fig. 2. While first-principles calculations have provided reliable information regarding structural and magnetic ground state properties for real (correlated or not) systems, they are known to generically fail to capture dynamical electron–electron correlation effects, and so they cannot access low-energy Kondo quasiparticles and Mott localization as well as the emergence of Hubbard satellites (local moments) at high energies [47]. Combining DFT with DMFT is a many-particle prescription for overcoming this problem [38]. Thus, within

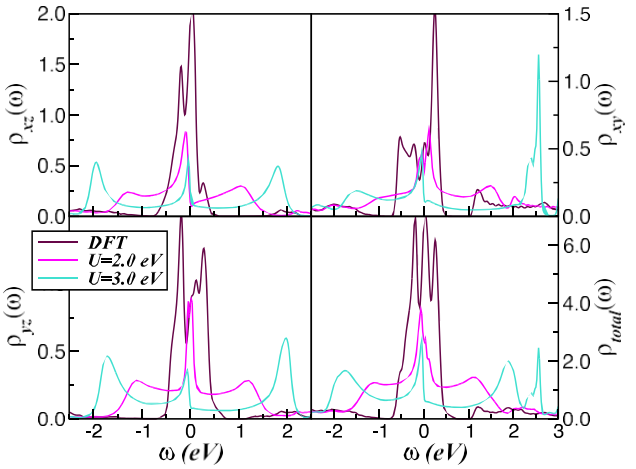

Fig. 2 Comparison between the GGA and GGA+DMFT orbital-resolved and total Cr 3*d*–t_{2g} density of states (DOS) of paramagnetic CrSBr bulk crystal. Important features to be seen is the narrow bare DFT bandwidth, the changes in the DFT-t_{2g} electronic states, and the correlated electronic structure reconstruction shown in the DFT+DMFT results with increasing on-site Coulomb interaction U

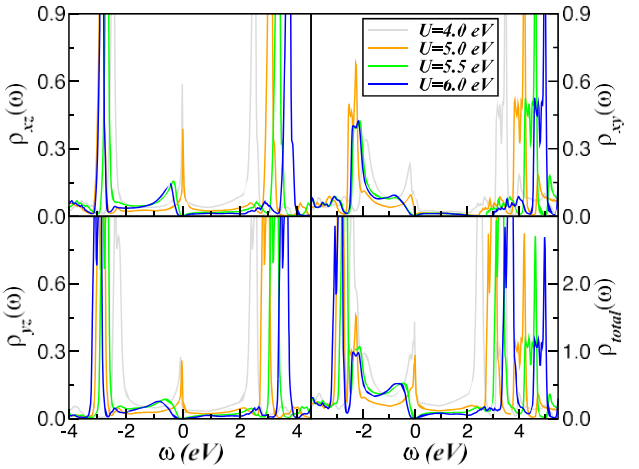

Fig. 3 Evolution of the GGA+DMFT orbital-resolved and total spectral functions of paramagnetic CrSBr across the correlation-driven Mott metal–insulator transition. Notice the orbital-selective suppression of the narrow Kondo quasiparticles in metallic CrSBr and the dynamical transfer of spectral weight from low energies to the Hubbard bands

GGA the one-electron part of the MO Hamiltonian for CrSBr reads $H_0 = \sum_{\mathbf{k},a,\sigma} \epsilon_a(\mathbf{k}) c^\dagger_{\mathbf{k},a,\sigma} c_{\mathbf{k},a,\sigma}$, where a = *xz, yz, xy* denote the diagonalized t_{2g} orbitals and $\epsilon_a(\mathbf{k})$ is the corresponding band dispersion, which encodes details of the real one-electron band structure. These three Cr-3*d* orbitals are the relevant one-particle inputs for MO-DMFT which generates a Mott–Hubbard insulating state as shown below. Local MO interactions in CrSBr are contained in $H_{int} = U \sum_{i,a} n_{i,a,\uparrow} n_{i,a,\downarrow} + U' \sum_{i,a\neq b} n_{i,a} n_{i,b} - J_H \sum_{i,a\neq b} \mathbf{S}_{i,a} \cdot \mathbf{S}_{i,b}$. Here, U is the on-site Coulomb interaction, $U' = U - 2J_H$ is the interorbital Coulomb interaction term, and J_H is the Hund's coupling. We evaluate the many-particle Green's functions of the MO Hamiltonian $H = H_0 + H_{int}$ within DFT+DMFT [38], using MO iterated perturbation theory (MO-IPT) as impurity solver [48]. The DMFT solution involves replacing the lattice model by a self-consistently embedded MO-Anderson impurity model, and the self-consistency condition requiring the local impurity Green's function to be equal to the local Green's function for the lattice. The full set of equations for the MO case can be found in Ref. [48], so we do not repeat the equations here.

Let us now turn our attention to our DFT+DMFT results obtained within the formal Cr^{3+} oxidation state of the CrSBr parent compound. In Fig. 2, we display the effect of MO dynamical correlations on the orbital-resolved $[\rho_{a,\sigma}(\omega)]$ and total $[\rho_{total}(\omega) = \sum_{a,\sigma} \rho_{a,\sigma}(\omega)]$ t_{2g} DOS of orthorhombic CrSBr, showing orbital-selective Kondo quasiparticle peaks [47] develops at or near E_F in the t_{2g} DOS, followed by the emergence of incoherent upper (UHB) and lower (LHB) Hubbard bands at high energies, a feature that to the best of our knowledge has not been reported in the extant literature of CrSBr bulk or low-D crystals. Also interesting in Fig. 2 is the pseudo-bandgap and the narrow UHB at U = 3.0 eV that develop in the electronic state with *xy* orbital character, signaling its close proximity to Mott localization. Taken together, the interplay between many-particle, electron–electron interactions and the clear differences in bare electronic lineshape near E_F are important seeds toward correlated electronic structure reconstruction and Mott localization of CrSBr vdW bulk crystal, as shown below.

In Fig. 3, we display the orbital-resolved and total DOS across the Mott metal–insulator transition of CrSBr. We recall here that strongly correlated many-particle systems are paramagnetic Mott insulators, where all orbital sectors display a Mott–Hubbard gap at E_F [50]. In spite of orbital-selective suppression of the narrow Kondo quasiparticles, transfer of spectral weight from low energies to the Hubbard bands at high energies is visible in a more or less pronounced way in Fig. 3, depending on the orbital character, within the t_{2g} orbital-resolved spectral functions. This behavior highlights the intrinsic tendency toward large transfer of spectral weight in transition metal compounds [50], where the correlation to bandwidth (U/W) ratio is sizable [51].

selective electronic structure reconstruction induced by

MO elecron–electron correlation effects with pronounced changes in the t_{2g} orbitals, both near E_F and at high energies. At $U = 2.0$ eV and fixed $J_H = 0.7$ eV (a value close to that reported in Ref. [49]), orbital-

To shine additional light onto the effect of MO electron–electron interactions in CrSBr, we show in Fig. 4 the frequency dependence of the orbital-resolved self-energies of the imaginary (main panels) and real (insets) parts for the U values considered in Fig. 3. At $U = 4.0$ eV, $Im\Sigma_a(\omega)$ shows ω^2-dependence character-

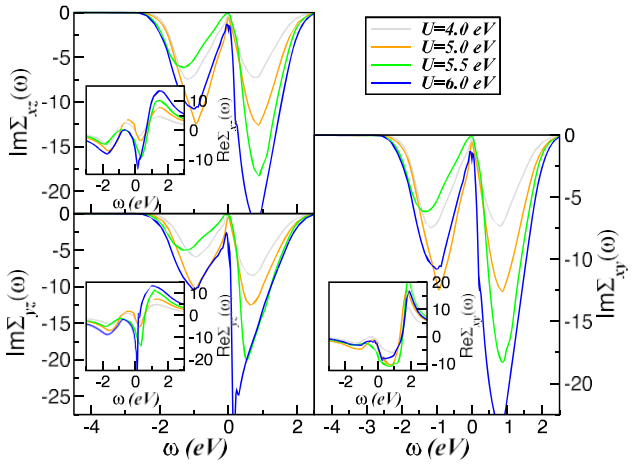

Fig. 4 Orbital-resolved self-energies imaginary (main panels) and real (insets) parts of CrSBr bulk crystal, showing their evolution with increasing the on-site Coulomb interaction U. Particular features to be seen is the particle–hole asymmetry and the presence of a pole in the yz self-energy near E_F, a fingerprint of the Mott insulating state

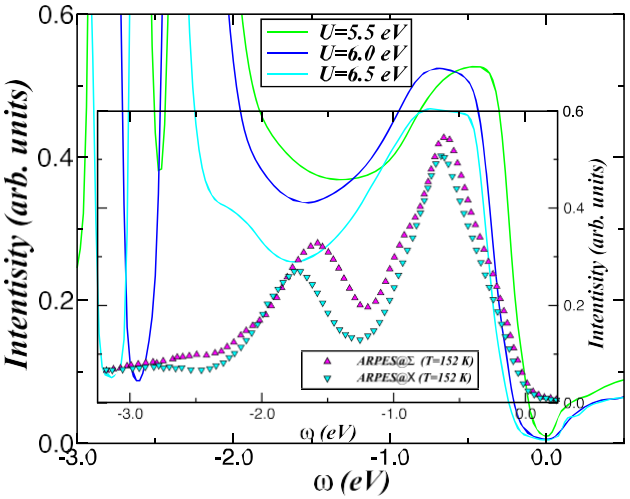

Fig. 5 Evolution of the DFT+DMFT total DOS in the Mott–Hubbard electronic localized state of paramagnetic CrSBr bulk crystal (main panel) with increasing on-site Coulomb repulsion U. The inset displays the angle-resolved photoemission spectroscopy (ARPES) data recorded at 152 K on two different **k**-directions [12]. Notice the qualitative theory–experiment agreement, particularly for the position of the low-energy shoulder, followed by a peak–dip–hump lineshape

istic of Fermi liquid metals. However, as shown in Fig. 3, this canonical correlated electronic fingerprint evolves into an orbital-selective state at $U = 5.0$ eV with coexisting insulating (xy) and metallic (xz, yz) channels. Due to orbital-selective Mottness, at $U = 5.0$ eV, the xy orbital now acts as a localized moment to the xz, yz channels responsible for the emergence of incoherent metallicity via U', J_H -induced interorbital proximity effect. This in turn indicates the presence of strong MO correlations within the orbital-selective metallic phase of CrSBr. Comparing our results with that of CrX_3 vdW crystals [36, 37], among other correlated systems [52, 53], we notice similar features in CrSBr, i.e., the strong particle–hole asymmetry in $\Sigma_a(\omega)$. This particle–hole asymmetry is manifested by the appearance of a peak above E_F in $Im\Sigma_a(\omega)$, which becomes more particle–hole asymmetric in the Mott phase of paramagnetic CrSBr. Importantly, as can be seen in the insets of Fig. 4, the self-energy real parts of the Mott localized components have pronounced frequency dependence near E_F, which indicates that the bare electronic states are strongly renormalized by the orbital-resolved self-energy real parts, stabilizing the Mott insulating state as in bct NbO_2 [52].

To see whether our results for the Mott–Hubbard insulating state of CrSBr are consistent with extant spectroscopy data, in Fig. 5 we show the DFT+DMFT results (main panel) and angle-resolved photoemission spectroscopy (ARPES) data [12] recorded at 152 K on two different **k**-directions (inset). As seen, good qualitative agreement between theory and experiment is found over the entire range of -1.5 eV $\leq \omega \leq E_F$. In particular, the peak–dip–hump and the energy position of the incoherent low-energy excitation are close to -0.6 eV below E_F, which agrees with the total t_{2g} spectral function. Thus similar to Ref. [54], our results in the main sentation of the valence one-electron band structure of paramagnetic CrSBr near E_F and its link to **k**-resolved spectral functions. Albeit with reduced intensity, our results qualitatively reproduce the shoulder feature centered around 1.6 eV below E_F in the experiment. Thus, for CrSBr, incoherent components with distinct orbital (see Fig. 5) and **k**-resolved electronic lineshape are visible at low to moderate binding energies, in spite of large-scale spectral weight transfer induced by sizable electron–electron interactions. Interestingly in this context is the crossing point seen in the experimental curves at -2.0 eV binding energy, a fingerprint of dynamical transfer of spectral weight. Finally, looking at both the conduction and valence band states close to E_F reveals an U-shaped like bandgap similar to that seen in Ref. [15]. Future angle-integrated photoemission spectroscopy (PES) and inverse PES are called for to corroborate our electronic structure evolution for the Mott localized electronic state of paramagnetic CrSBr.

Electron localization probed in extant transport experiments [2, 15, 27] may provide additional support to our t_{2g} orbital-selective electronic structure reconstruction of stoichiometric CrSBr. Specifically, we study the T-dependence of the dc resistivity and correlate it with the Mott scenario derived above. Given the DFT+DMFT many-particle spectral functions $\rho_a(\mathbf{k}, \omega) = -\frac{1}{\pi} ImG_a(\mathbf{k}, \omega)$ the (static) dc conductivity $[\sigma_{dc}(T)]$ [55] can be expressed as $\sigma_{dc}(T) = \frac{2\pi e^2}{kV} \sum_a \int d\epsilon \rho_a^{(0)}(\epsilon) \int d\omega \rho_a^2(\epsilon, \omega)[-f'(\omega)]$. In this expression, $\rho_a^{(0)}(\epsilon)$ is the bare DFT DOS of the a-orbitals (Fig. 2), V is the unit cell volume, and $f(\omega)$

panel of Fig. 5 represents a qualitatively accurate repre-

is the Fermi function. As in Ref. [56], the approxima-

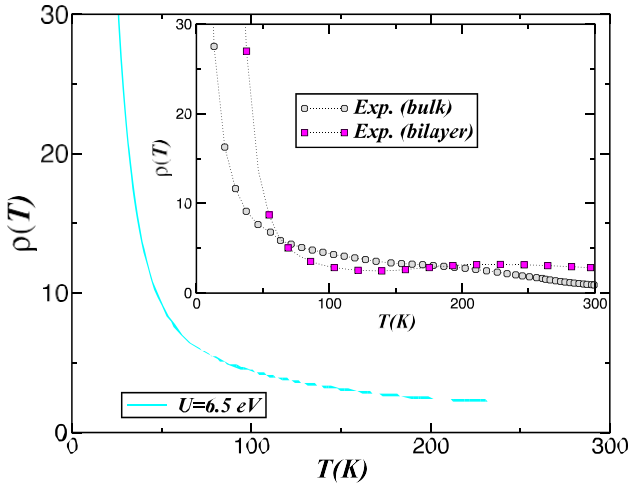

Fig. 6 Temperature dependence of the electrical resistivity obtained using the DFT+DMFT. Inset shows the resistivity data of bulk [15] and bilayer [2] CrSBr. Noteworthy is the qualitative good theory–experiment agreement from low- to room-T

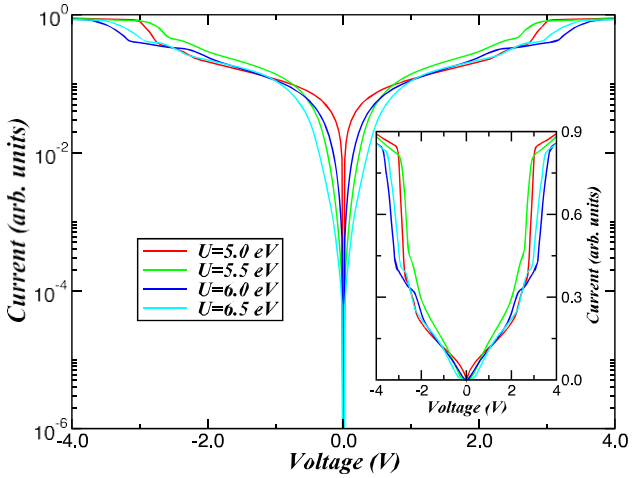

Fig. 7 Evolution of the semi-logarithmic (main panel) and linear (inset) $I-V$ curves of paramagnetic CrSBr bulk crystal on increasing the on-site Coulomb interaction U. Notice the minimal memristive behavior in the inset and the ON/OFF ratio as high as 10^4 at the main panel, supporting the bipolar switching with stable low resistance state (LRS) and high resistance state (HRS) reported in experiment [29]

tion made here is to ignore the **k**-dependence of electron's velocity, $v_{\mathbf{k},a}$. In this situation, following Saso et al. [57, 58], we approximate $v_{\mathbf{k},a}$ by a single average carrier velocity (v) for the t_{2g} orbitals of CrSBr. In fact, Refs. [57, 58] and [59] have shown that this assumption works well for numerical computations of $\sigma_{ac}(\omega)$ for Kondo insulators (FeSi and YbB_{12}), V_2O_3, and Fe-pnictide superconductors, supporting our approximation in $\sigma_{dc}(T)$ above. The observed features in resistivity $\rho_{dc}(T) \equiv 1/\sigma_{dc}(T)$ originated from correlation induced spectral changes: Showing how this provides a qualitative description of extant experimental data is our focus here. In Fig. 6, we show the T-dependence of the resistivity $\rho(T)$ computed using the $U = 6.5$ eV DFT+DMFT spectral function of paramagnetic CrSBr shown in Fig. 5. As seen in Fig. 6, the DFT+DMFT result for the CrSBr parent compound shows an insulating behavior from room-T down to 25 K. As seen, our result for $U = 6.5$ eV in Fig. 6 is in good qualitative accord with that reported for both bulk [15] and bilayer [2] CrSBr parent compound (see the inset of Fig. 6), providing support to our Mott–Hubbard localized electronic state.

Finally, to shine light on the role played by MO electron–electron correlation effects into the changes in the Cr-based current–voltage ($I-V$) characteristic of CrSBr memristor [29], in Fig. 7 we present our results computed using the DFT+DMFT spectral functions for the different U values considered in Figs. 3 and 5. Firstly, we shall point out here that within the wide-band limit of the left (L) and right (R) electrodes, the current formula for a tunneling experiment can be written as $I = \frac{4e}{\hbar}\sum_{a,\sigma}\int d\omega\, \tilde{\Gamma}(\omega)\,\{f_L(\omega) - f_R(\omega)\}\,\rho_{a,\sigma}(\omega)$ $\Gamma_L(\omega)+\Gamma_R(\omega)$. $f_a(\omega) = 1/(e^{\beta(\omega-\mu_a)}+1)$ and $\rho_{a,\sigma}(\omega) = -\frac{1}{\pi}\,\mathrm{Im}\,G_{a,\sigma}(\omega)$ are, respectively, the Fermi function of the electrode α and the total DOS of the Cr-3d t_{2g} channel with spin-σ of paramagnetic CrSBr. Secondly, for simplicity we assume a symmetric voltage drop, $\mu_L = -\mu_R = eV$, and the wideband limit with constant DOS for the leads. Without loss of generality, these assumptions allows for a microscopic rationalization of the $I-V$ characteristic of paramagnetic CrSBr memristor [29].

In the main panel and at the inset of Fig. 7, we show, respectively, the semi-logarithmic and linear current–voltage ($I - -V$) curves obtained using the total DFT+DMFT spectral functions shown in Figs. 3 and 5. As seen, at small V, paramagnetic CrSBr exhibits minimal memristive behavior as reported in experiment [29], which goes over to a memristive switching where the resistance steady-state value exhibits an ON/OFF (or SET/RESET) ratio as high as 10^4 assisted by U-driven dynamical transfer of spectral weight. Taken together with the experimental result of Ref. [29], this behavior indicates that paramagnetic CrSBr memristor exhibits analog resistive memory with a bipolar low resistance state (LRS) and high resistance state (HRS) similar to that seen in experiments for MoS_2 [64–66]. According to our DFT+DMFT results, this intrinsic dual-terminal [29], bipolar switching is due to selective orbital reconstruction, thus proving a volatile memristive functionality in contrast to the nonvolatile electric response of antiferromagnetic CrSBr [27], both however being relevant for future CrSBr memory-based, brain-inspired neuromorphic computing.

[60–61], where $\tilde{\Gamma}(\omega) = \Gamma_L(\omega)\Gamma_R(\omega)/\Gamma(\omega)$ with $\Gamma_\alpha(\omega) = \pi \sum_k |t_k^\alpha|^2 \delta(\omega - \varepsilon_{k\alpha})$ being the coupling strength between electrode α and the central region [62, 63], and $\Gamma(\omega) =$

3 Conclusion

In summary, in this work, we have performed GGA and GGA+DMFT calculations for understanding the electronic structure reconstruction of bulk CrSBr crystal in its non-magnetically ordered state. Using realistic Coulomb interaction parameters in the three-orbital Hubbard model of CrSBr, we provide a microscopic description of the excitation spectrum and the Mott localized state which emerges in this vdW lattice system. The central message of our approach is to show that a strong coupling [51] picture leads to a qualitative description for the low-energy shoulder feature in ARPES [12], the T-dependence of electrical resistivity for bulk [15] and bilayer [2] as well as the memristor $I--V$ characteristic [29] of CrSBr in a single theoretical picture. Taken together, our comparative theory–experiment analysis provides support for the correlated nature of Cr-based parent compound [51, 67, 68], and it is expected to be generally applicable to understanding orbital selectivity in correlated systems and the underlying electronic state which emerges in vdW materials [69].

Acknowledgement (L.C., S.S.C., E.F.C., and A.R.C.) is made to CNPq and CAPES. S.L. thanks the Leverhulme Trust for support under Project No. RPG-2020-052. The authors thank Byron Freelon for valuable comments and discussions.

Author contributions

SSC carried out the DFT calculations. LC designed and carried out the DFT+DMFT study. The authors contributed to the scientific discussions and the preparation of the manuscript, and approved the final version of the manuscript.

Data Availability Statement This manuscript has no associated data or the data will not be deposited. [Author's comment: The datasets generated and analyzed during the current study are available from the corresponding author upon reasonable request.]

Code Availability Statement This manuscript has no associated code/software. [Author's comment: Code/Software sharing not applicable to this article as no code/software was generated or analysed during the current study.]

References

1. K.S. Novoselov et al., Science **306**, 666 (2004)
2. M.E. Ziebel et al., Nano Lett. **24**, 4319 (2024)
3. A.K. Geim, I.V. Grigorieva, Nature **499**, 419 (2013)
4. B. Huang et al., Nature **546**, 270 (2017)
5. B. Huang et al., Nat. Nanotechnol. **13**, 544 (2018)
6. C. Gong et al., Nature **546**, 265 (2017)
7. D. Zhong et al., Sci. Adv. **3**, 1603113 (2017)
8. M. Gibertini, M. Koperski, A.F. Morpurgo, K.S. Novoselov, Nat. Nanotechnol. **14**, 408 (2019)
9. K.S. Burch, D. Mandrus, J.G. Park, Nature **563**, 47 (2018)
10. F. Wu et al., Adv. Mater. **34**, 2109759 (2022)
11. N.P. Wilson et al., Nat. Mater. **20**, 1657 (2021)
12. M.D. Watson, et al., NPJ 2D Mater. Appl. **8**, 54 (2024)
13. C.S. de Brito et al., Nano Lett. **23**, 11073 (2023)
14. E.J. Telford et al., Nat. Mater. **21**, 754 (2022)
15. E.J. Telford et al., Adv. Mater. **32**, 2003240 (2020)
16. O. G¨oser, W. Paul, H.G. Kahle, J. Magn. Magn. Mater. **92**, 129 (1990)
17. T. Xu, X. Zou, J. Phys. Chem. Lett. **11**, 3152 (2020)
18. K. Lee et al., Nano Lett. **21**, 3511 (2021)
19. W. Liu et al., ACS Nano **16**, 15917 (2022)
20. S.A. L´opez-Paz et al., Nat. Commun. **13**, 4745 (2022)
21. T.M.J. Cham et al., Nano Lett. **22**, 6716 (2022)
22. F. Moro et al., Adv. Funct. Mater. **32**, 2207044 (2022)
23. A. Scheie et al., Adv. Sci. **9**, 2202467 (2022)
24. J. Beck, ZAAC, J. Inorg. Gen. Chem. **585**, 157 (1990)
25. J. Klein et al., ACS Nano **17**, 5316 (2023)
26. Z. Liu, et al. arXiv:2407.13230 (unpublished)
27. J. Jo, L.E. Hueso et al., Nano Lett. **24**, 4471 (2024)
28. B. Yang et al., Nat. Commun. **15**, 4459 (2024)
29. Z. Li et al., J. Mater. Sci. Mater. Electron. **35**, 1091 (2024)
30. Y. Wang, N. Luo, J. Zeng, L.-M. Tang, K.-Q. Chen, Phys. Rev. B **108**, 054401 (2023)
31. H.-T. Guo, S.-D. Guo, Y. S. Ang. arXiv:2308.03430 (unpublished)
32. L. Craco, S.S. Carara, Condens. Matter. **10**, 27 (2025)
33. X. Bo, F. Li, X. Xu, X. Wan, Y. Pu, New J. Phys. **25**, 013026 (2023)
34. K. Yang, G. Wang, L. Liu, D. Lu, H. Wu, Phys. Rev. B **104**, 144416 (2021)
35. M. Bianchi et al., Phys. Rev. B **107**, 235107 (2023)
36. L. Craco, S.S. Carara, Y.-C. Shao, Y.-D. Chuang, B. Freelon, Phys. Rev. B **102**, 195130 (2020)
37. L. Craco, S.S. Carara, Y.-C. Shao, Y.-D. Chuang, B. Freelon, Phys. Rev. B **103**, 235119 (2021)
38. G. Kotliar et al., Rev. Mod. Phys. **78**, 865 (2006)
39. J.M. Soler et al., J. Phys. Condens. Matter **14**, 2745 (2002)
40. J.P. Perdew, K. Burke, M. Ernzerhof, Phys. Rev. Lett. **77**, 3865 (1996)
41. N. Troullier, J.L. Martins, Phys. Rev. B **43**, 1993 (1991)
42. W. Kohn, L.J. Sham, Phys. Rev. **140**, A1133 (1965)
43. J. Junquera, Ó. Paz, D. S´anchez-Portal, E. Artacho, Phys. Rev. B **64**, 235111 (2001)
44. J. Moreno, J.M. Soler, Phys. Rev. B **45**, 13891 (1992)
45. H.J. Monkhorst, J.D. Pack, Phys. Rev. B **13**, 5188 (1976)
46. F. Pei et al., Adv. Func. Mater. **34**, 2309335 (2024)
47. A. Georges, G. Kotliar, W. Krauth, M.J. Rozenberg, Rev. Mod. Phys. **68**, 13 (1996)
48. L. Craco, Phys. Rev. B **77**, 125122 (2008)
49. O. Besbes, S. Nikolaev, N. Meskini, I. Solovyev, Phys. Rev. B **99**, 104432 (2019)
50. M. Imada, A. Fujimori, Y. Tokura, Rev. Mod. Phys. **70**, 1039 (1998)
51. I. Pollini, Phys. Rev. B **50**, 2095 (1994)

52. W.H. Brito, M.C.O. Aguiar, K. Haule, G. Kotliar, Phys. Rev. B **96**, 195102 (2017)
53. H. Park, R. Nanguneri, A.T. Ngo, Phys. Rev. B **101**, 195125 (2020)
54. L. Craco, S. Leoni, Phys. Rev. B **108**, 045140 (2023)
55. C. Grenzebach, F.B. Anders, G. Czycholl, Phys. Rev. B **74**, 195119 (2006)
56. L. Craco, S. Leoni, Sci. Rep. **5**, 13772 (2015)
57. K. Urasaki, T. Saso, J. Phys. Soc. Jpn. **68**, 3477 (1999)
58. T. Saso, J. Phys. Soc. Jpn. **73**, 2894 (2004)
59. L. Baldassarre et al., Phys. Rev. B **77**, 113107 (2008)
60. Y. Meir, N.S. Wingreen, Phys. Rev. Lett. **68**, 2512 (1992)
61. L. Craco, K. Kang, Phys. Rev. B **59**, 12244 (1999)
62. G. Cuniberti, L. Craco, D. Porath, C. Dekker, Phys. Rev. B **65**, 241314(R) (2002)
63. X.-X. Bao, X.-F. Wang, Int. J. Quant. Chem. **1**, e27251 (2023)
64. M. Kim et al., Nat. Comms. **9**, 2524 (2018)
65. B. Tang et al., Nat. Commun. **13**, 3037 (2022)
66. P. Liu et al., Appl. Phys. Lett. **121**, 233501 (2022)
67. P. Jiang et al., Phys. Rev. B **99**, 144401 (2019)
68. S. Feldkemper, W. Weber, Phys. Rev. B **57**, 7755 (1998)
69. M. Gibertini, M. Koperski, A.F. Morpurgo, K.S. Novoselov, Nat. Nanotechnol. **14**, 408 (2019)